Applied Physics, Material Sciences, and Engineering Journal
ISSN 3065-1425
Volume 13 Issue 2
April-June 2025
Impact Factor: 8.13
Enquiry: contact@continentalpub.online
Published by Continental Publication | https://cspjournals.org/index.php/apmsej

EXPLORING TANTALUM'S MELTING MECHANISM AT HIGH PRESSURE WITH X-RAY DIFFRACTION AND AB INITIO DYNAMICS

Xiaoyan Ming Zhao
Institute of Applied Physics and Computational Mathematics, Beijing 100094, People's Republic of China

Abstract: *Understanding the melting behavior of tantalum under extreme pressures is critical for both fundamental science and high-energy-density applications. In this study, we investigate tantalum up to 450 GPa by integrating in situ X-ray diffraction measurements with ab initio molecular dynamics (AIMD) simulations. Experimental data confirm that the body-centered cubic (bcc) phase persists up to at least 318 GPa, as indicated by the continued presence of Ta(110), Ta(200), and Ta(211) diffraction peaks. These structural observations are consistent with recent high-pressure studies. The melting curve was computed using AIMD based on density functional theory, avoiding reliance on empirical potentials. The results align well with prior first-principles predictions and highlight the inadequacy of empirical models across wide pressure-temperature regimes. This combined experimental and computational methodology provides a reliable approach for investigating high-pressure phase stability and melting behavior in refractory metals, with broad implications for materials exposed to extreme conditions.*

Keywords: *Tantalum, high pressure, melting curve, ab initio simulations*

I. INTRODUCTION

Tantalum (Ta) is a representative element for understanding material properties and has diverse technological applications.[1–6] The high-pressure melting curve[7–28] and crystal structure before melting[8, 15, 16, 18, 19, 27, 29–32] of tantalum pose major challenges, requiring a reassessment of experimental and theoretical approaches. Discrepancies between dynamic and static compression experiments, as well as among theoretical studies, remain a key issue. Figure 1 highlights these inconsistencies, with a detailed review in Sec. S1 of the supplementary material.

Numerous experimental efforts have been dedicated to studying the melting curve of tantalum, utilizing both dynamic[7–11] and static[12–17] methods. However, the data in Fig. 1 show significant variation across studies. Recently, Kraus et al.[8] conducted in situ x-ray diffraction under shock compression to examine tantalum's crystal structure and melting behavior. They proposed a new melting curve based on their results, but it still differed notably from most dynamic experimental data in Fig. 1. These inconsistencies raise questions about the reliability of the repoerted melting curves.

Extensive theoretical studies have explored the melting of tantalum,[18–28] producing widely scattered melting curves in Fig. 1. First-principles simulations[19,20] generally agree with dynamic experiments[10,11]

Vol. 13 No. 2 | Imp. Factor: 8.13
DOI: https://doi.org/10.5281/zenodo.15845923

at higher pressures, while empirical models[22,23,27,28] align with static experiments at lower pressures.[14,16] To improve accuracy,

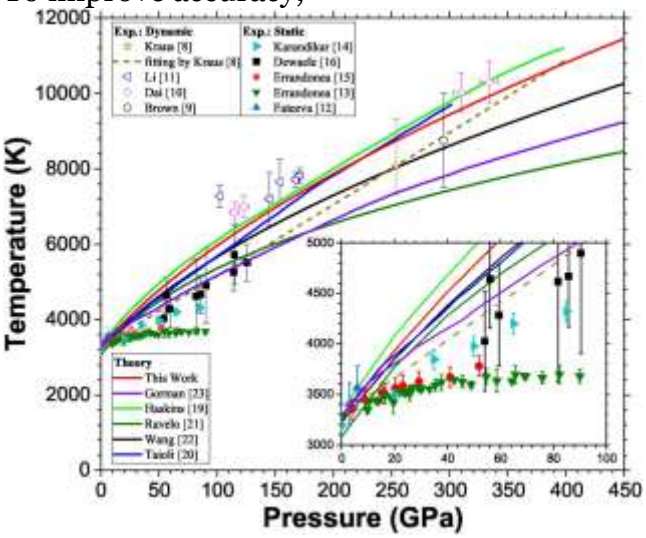

FIG. 1. Melting curves and points of tantalum from representative theoretical and experimental studies. The solid red line shows the melting curve from this study. The purple, light green, dark green, black, and blue lines correspond to theoretical models or simulations by Gorman et al.,[23] Haskins and Moriarty,[19] Ravelo et al.,[21] Wang et al.,[22] and Taioli et al.,[20] respectively. Solid symbols represent static experimental results from Refs. 12–16, while open symbols represented dynamic experimental results from Refs. 8–11. The dashed yellow line represents the fitting from Ref. 8. The inset enlarges the 0–100 GPa melting data for clarity.

various computational methods have been developed. Haskins and Moriarty[19] used model generalized pseudopotential theory (MGPT) molecular dynamics, combining the two-phase and Z-method, to calculate the melting curve up to 400 GPa. Taioli et al.[20] applied density functional theory (DFT)-based thermodynamic perturbation theory to study melting from 0 to 300 GPa. Gorman et al.[23] constructed an equation-of-state model using Hugoniot, ambient pressure heating, and ramp compression data up to 2.3 TPa. Despite these efforts, a precise melting curve considering the solid–liquid coexistence state has yet to be established from ab initio molecular dynamics (AIMD).

The crystal structure prior to melting is crucial for understanding melting curves. Theoretical studies proposed that tantalum may adopt orthorhombic structures (e.g., Pnma) under high pressure.[18,19,27,29,31,33] However, both static and dynamic compression experiments[8,15,16,30,32,34,35] consistently observe only the bodycentered cubic (BCC) phase, with no evidence of orthorhombic transitions. Kraus et al.[8] confirmed the persistence of the BCC phase up to shock melting using in situ x-ray diffraction. To assess the Pnma structure, they estimated the density assuming the observed peak corresponded to its strongest reflection. A 4%–6% deviation from experimental values, exceeding the 1% uncertainty, led to the exclusion of the Pnma phase. Despite this experimental consensus, discrepancies persist between the theoretical models and experimental observations, highlighting the need for further investigation to reconcile these differences.

In this study, we investigated the melting behavior of tantalum under high pressure. In situ x-ray diffraction measurements confirmed that tantalum did not adopt the Pnma structure and retained its BCC structure until shock melting. To determine the melting temperature, we used a precise and reliable AIMD simulation based on DFT. This method incorporated the experimentally constrained BCC structure and combined the strengths of the two-phase method and the modified-Z method.

Vol. 13 No. 2 | Imp. Factor: 8.13
DOI: https://doi.org/10.5281/zenodo.15845923

Considering in situ x-ray diffraction and sound velocity data, we estimated the shock melting pressure range for tantalum to be 255–318 GPa.

II. METHODS

Accurately determining the melting curve requires robust experimental and theoretical methods. This study combines in situ x-ray diffraction and AIMD simulations. Sections II A–II B detail these methods.

A. Crystal structure determination through insitu x-ray diffraction

Laser-driven shock compression experiments were conducted at the 10 kJ-class Laser Facility[36,37] of the Laser Fusion Research Center (LFRC), as illustrated in Fig. 2. The facility employs a 351 nm, nine-beam laser system, delivering up to 1 TW per beam onto millimeter-scale targets. The target assembly comprised an 8-μm-thick tantalum foil, sandwiched between a 50-μm-thick poly-

styrene (CH) ablator and a 120-μm-thick single-crystal lithium fluoride (LiF) window. A 0.5 μm adhesive layer bonded the components. To facilitate velocimetry measurements using a velocity

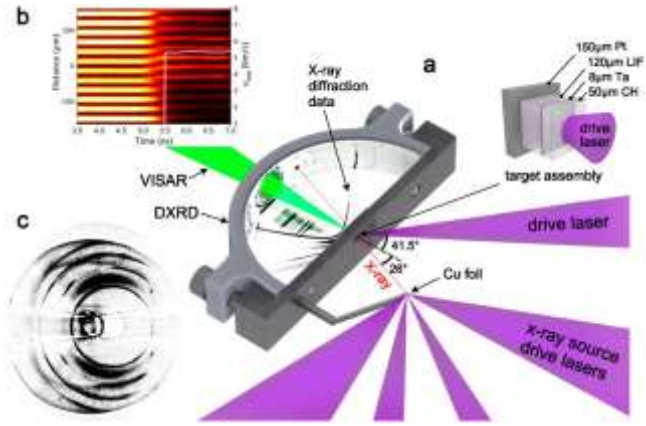

FIG. 2. Experimental configuration of in situ x-ray diffraction on the 10 kJ-class laser facility. (a) Schematic of the diagnostic setup and target assembly. The target consists of an 8μm Ta foil sandwiched between a 50-μm CH ablator and a 120-μm LiF window, bonded by a 0.5-μm adhesive layer. Four auxiliary laser beams (200 μm spot size, 0.4 kJ/beam) irradiate a 10-μm Cu foil to generate an 8.4 keV x-ray source, which probes the shocked Ta sample. Diffraction patterns were recorded on image plates (IPs) within the dynamic x-ray diffraction detector (DXRD). (b) Velocity history of the Ta–LiF interface measured by a velocity interferometer system for any reflector (VISAR). (c) Representative stereographic projection of x-ray diffraction data at 318 GPa.

interferometer systems for any reflector (VISAR),[38] the rear surface of the LiF window was coated with a 100 nm aluminum layer to enhance reflectivity at the Ta–LiF interface.

One of the nine beams was incident at 41.5 from the target normal, with a 3 mm focal spot and pulse energy between 0.5 and 2 kJ, estimated using scaling laws. Continuous phase plates were employed to homogenize the laser intensity spatially. The pulse shape was tailored to maintain a near-constant pressure on the target over several nanoseconds. A steady shock wave was launched in the CH ablator and transmitted into the tantalum sample. To generate an x-ray backlighter, four additional beams were directed onto one side of a 10-μm-thick copper foil, located 30 mm from the target at a 26 angle. These beams, each delivering 0.4 kJ and focused to a 200 μm spot, produced 8.4 keV quasi-monochromatic He-α radiation with 1% bandwidth. The laser pulse included a 1 ns pre-pulse (10% of total energy) preceding a 0.5 ns main pulse by 2 ns. The resulting x-ray emission illuminated the sample at the midpoint of the shock propagation.

Vol. 13 No. 2 | Imp. Factor: 8.13
DOI: https://doi.org/10.5281/zenodo.15845923
In laser shock experiments, in situ x-ray diffraction have been widely used to monitor the crystal structure under high pressure.[39–48] To precisely determine tantalum's structure before shock melting, we optimized the detector to improve sensitivity and signal-to-noise ratio. Time-resolved x-ray diffraction patterns were collected in transmission geometry using image plates (IPs) mounted within a cylindrical dynamic x-ray diffraction detector (DXRD). The target was aligned with a 400-μm-diameter platinum (Pt) pinhole positioned at the front of a Φ6414 mm half-cylinder enclosure, serving as the DXRD chamber. A 12 mm rear aperture allowed simultaneous VISAR access. To improve the accuracy of d-spacing measurements, the unshocked portion of the sample and the Pt pinhole provided reference diffraction lines. Copper foils (10 μm thick) were affixed to the IPs to filter out thermal background emission. The d-spacing uncertainty was quantified based on the angular resolution of the diffraction setup (2θ) and the bandwidth of the x-ray source.

Shock velocities were determined using a VISAR, with the Ta–LiF interface velocity used to infer pressure via the impedance matching method[49–52] in eight of ten shots. The remaining two shots employed the free-surface velocity approximation,[53] assuming the free-surface velocity is twice the particle velocity. To estimate the pressure at shock breakout, we averaged the velocity over 1 ns during steady shock conditions. The total pressure uncertainty was evaluated considering the following factors. (i) Temporal velocity variation, reflecting shock unsteadiness, was quantified using statistical deviations. (ii) Spatial velocity variation, due to non-uniform shock loading, was estimated from the maximum standard deviation across the target surface. (iii) VISAR diagnostics, where a 5% uncertainty in fringe shift was assumed. The etalon configurations (24, 22, and 17 mm) corresponded to velocity uncertainties of 0.104, 0.114, and 0.147 km/s, respectively. (iv) Hugoniot uncertainties, arising from both tantalum and LiF reference equations of state. This structured evaluation ensured a comprehensive and conservative assessment of pressure uncertainties in the experiment.

B. Melting curve simulations by abinitio molecular dynamics

Various methods[54–62] have been used to simulate melting phenomena. In this study, we employed a first-principles molecular dynamics approach that integrates the advantages of the two-phase method and the modified-Z method. This approach has proven effective in accurately predicting the melting curve of vanadium.[63] Here, we apply it for the first time to investigate the high-pressure melting curve of tantalum. Simulations were conducted using the Vienna ab initio simulation package (VASP),[64–67] a first-principles DFT-based projector augmented-wave method.[68] We adopted Mermin's finite temperature DFT implementation[69] and used a pseudopotential incorporating 11 valence electrons ($5p^6$, $5d^3$, and $6s^2$), along with the Perdew–Burke–Ernzerh of generalized gradient approximation[70,71] for electronic exchange-correlation. These parameters were selected based on their consistency with theoretical and experimental values for the lattice parameter and bulk modulus.[1,35] To ensure accuracy, we utilized a 5524 Wigner– Seitz supercell containing 600 atoms with periodic boundary conditions. Convergence was achieved with a total energy tolerance of 210^5 eV, considering the gamma point in the reciprocal space. The plane-wave energy cutoff was set to 300 eV. Simulations ran for 5–10 ps with a 1 fs time step. The melting points were determined by averaging the temperature and pressure of the solid–liquid coexistence state over an extended picosecond period.

III. RESULTS AND DISCUSSION

Applied Physics, Material Sciences, and Engineering Journal
Vol. 13 No. 2 | Imp. Factor: 8.13
DOI: https://doi.org/10.5281/zenodo.15845923

A. Structure of tantalum under high pressure by insitu x-ray diffraction measurements

Eleven in situ x-ray diffraction experiments were conducted, with shock stress ranging from ambient to 393 GPa along the principal Hugoniot of tantalum. Shock stress was determined using VISAR measurements of interface or free-surface velocity. Figure 3 shows the velocity-timehistory for all shots, normalized to a common starting time for direct comparison of shock wave evolution. The velocity

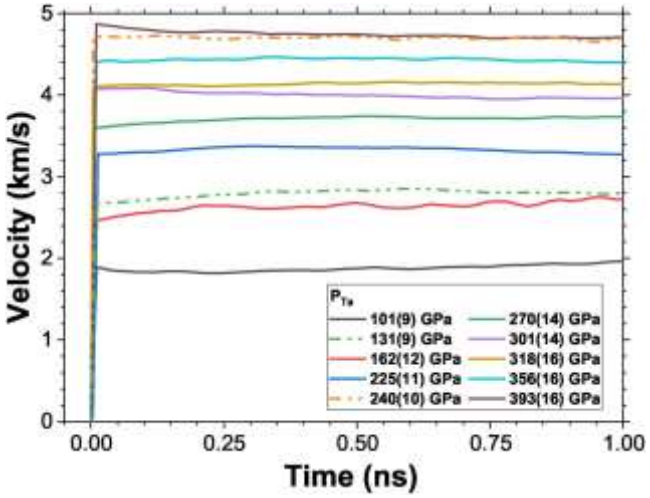

FIG. 3. Velocity-time history obtained from VISAR measurements. Solid and dashed line style represent different types of velocity, respectively: colored solid lines represent velocity-time history of Ta–LiF interface, while colored dashed dotted lines represent velocity-time history of the tantalum free surface.

b Density calculated from averaged lattice constant.

was averaged over a 1 ns window for each shot to calculate the corresponding stress. Raw velocity data and shot timing details were provided in Sec. S2 of the supplemental material. Table I listed the stress values and their uncertainties (k ¼ 1) for all shock compression shots.

A representative in situ x-ray diffraction pattern was shown in Fig. 4. Data were extracted from three separated IPs and regrouped from Cartesian coordinates to 2θ-f space. Diffraction lines were identified as ambient Pt, ambient Ta, and shock-compressed Ta. Using Bragg's law, diffraction angles were converted to d- spacing values with a precision of +0:12. Three diffraction lines from shock-compressed Ta were observed, which was critical for reliable structural analysis. The Pt(200) line was absent due to texturing effects, preventing its detection. Dewarped in situ x-ray diffraction images from 101 to 356 GPa were provided in Sec. S3 of the supplemental material.

Melting was identified through x-ray diffraction by observing the broadening of diffraction peaks at high pressures. Figure 5 presents diffraction lines from ambient to 393 GPa, shifted for clarity. Colors indicate different states: black for solid tantalum, red for solid–liquid coexistence, and blue for the liquid state. Shock melting was evident from the evolution of the compressed Ta(110) peak. Below 270 GPa, the Ta(110) lines displayed clear solid-state characteristics. As pressure increased, these lines broadened, showing a diffuse background alongside sharp solid peaks. At 356 and 393 GPa, the solid peak vanished, replaced by a single broad peak, indicating complete melting.

Vol. 13 No. 2 | Imp. Factor: 8.13
DOI: https://doi.org/10.5281/zenodo.15845923

The stability of tantalum's crystal structure prior to melting is critical for understanding its high-pressure melting behavior. In this study, we analyzed d-spacings derived from in situ x-ray diffraction data in Fig. 5 using

TABLE I. Summary of the in situ x-ray diffraction experiments of shock-compressed tantalum. d_{hkl} refers to d-spacing of reflection hkl, and a_0 was the lattice constant of the BCC structure. The uncertainties including measurement and propagation errors were given in parentheses at the 1σ level. The uncertainties in parentheses represent the last two digits of the values.

Shot No.	Stress (GPa)	d_{110} (Å)	d_{200} (Å)	d_{211} (Å)	a_0 (Å)[a]	ρ (g/cm³)[b]	Phase
20190704097	Ambient	2.344 (10)	1.659 (9)	1.352 (3)	3.316 (18)	16.47 (27)	BCC
20190708101	101 ± 9	2.122 (24)	1.509 (8)		3.009 (16)	22.05 (35)	BCC
20200716086	131 ± 9	2.097 (22)	1.486 (6)	1.241 (5)	2.969 (12)	22.97 (28)	BCC
20190705099	162 ± 12	2.064 (20)	1.456 (11)		2.915 (22)	24.25 (55)	BCC
20200708077	225 ± 11	2.006 (20)	1.425 (9)		2.843 (18)	26.14 (50)	BCC
20200717090	240 ± 10	2.002 (20)	1.409 (9)		2.825 (18)	26.67 (51)	BCC
20200717089	270 ± 14	1.998 (28)	1.403 (10)		2.816 (20)	26.92 (58)	BCC+Liquid
20200808117	301 ± 14	1.992 (43)	1.404 (11)		2.813 (22)	27.01 (63)	BCC+Liquid
20200715084	318 ± 16	2.000 (32)	1.397 (12)		2.811 (24)	27.05 (70)	BCC+Liquid
20200708075	356 ± 16						Liquid
20200716088	393 ± 16						Liquid

a Lattice constant and uncertainties were calculated by averaging the lattice constant values obtained from d_{110} and d_{200}.

Bragg's law, incorporating experimental uncertainties. For comparison, d-spacing

Vol. 13 No. 2 | Imp. Factor: 8.13
DOI: https://doi.org/10.5281/zenodo.15845923

values of Kraus et al.[8] were recalculated from their reported density measurements under shock compression, combined with an ideal BCC structural model. Reference values in Fig. 6 were generated by reconciling the tantalum Hugoniot pressure–density relationship with both BCC and orthorhombic (Pnma, Fddd, Cmcm, Pmma) structural models.

Notably, our diffraction data spanning 101 GPa to the shock melting at 318 GPa show excellent agreement with the BCC structure as illustrated in Fig. 6. No discontinuities in d-spacing or emergence

Vol. 13 No. 2 | Imp. Factor: 8.13
DOI: https://doi.org/10.5281/zenodo.15845923

of new diffraction lines were observed, ruling out previously proposed orthorhombic phases. While previous experiments[8,15,16,35] confirmed BCC stability up to 311 GPa under high

FIG. 4. Representative in situ x-ray diffraction pattern of Ta (shot No. 202007160, 131 + 9 GPa) projected to the 2 θ–f space, where f is the azimuthal angle around the incident x-ray direction. The red and green vertical dashed lines show positions of ambient Ta and ambient Pt x-ray diffraction peaks,

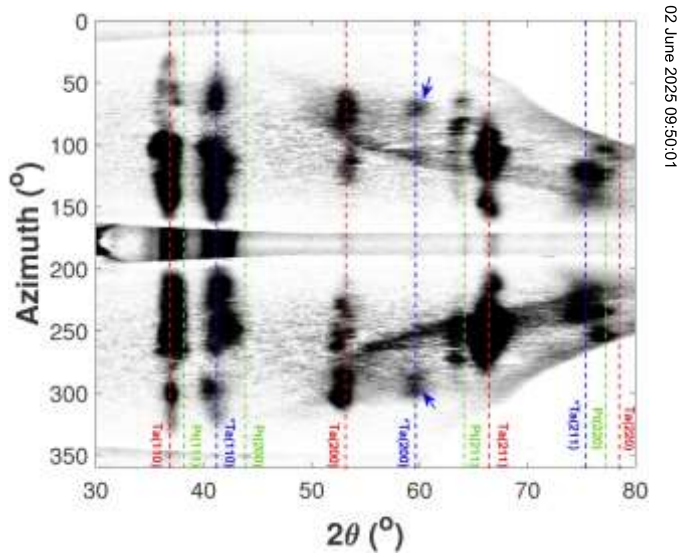

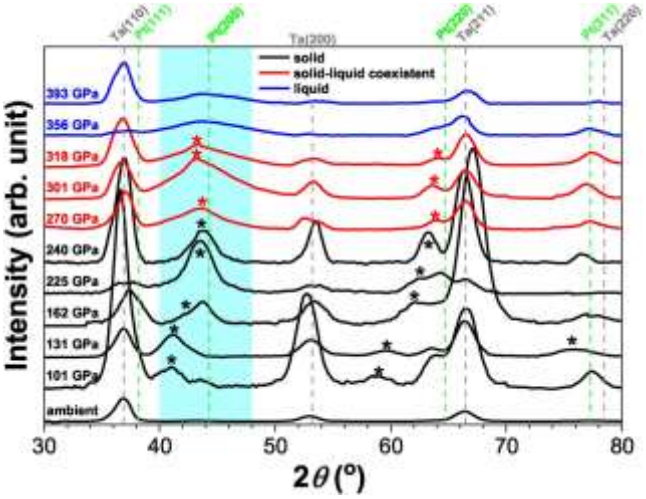

Vol. 13 No. 2 | Imp. Factor: 8.13
DOI: https://doi.org/10.5281/zenodo.15845923

FIG. 5. Diffraction lineouts of tantalum were plotted with vertical shifts and color grouping. Black lines represented solid phase lineouts, red lines indicated solid– liquid mixture phase lineouts, and blue lines represented liquid phase lineouts. Gray and green dashed lines marked the ambient tantalum and Pt reflections, respectively. Compressed Ta(110) peaks were observed between 40 and 48, exhibiting distinct solid diffraction characteristics below 270 GPa. Diffuse scattering appeared at 270 GPa, and the solid signature vanished at 356 GPa. Color-coded asterisks labeled the position of shock-compressed solid tantalum under different pressures. Raw data for lineouts can be found in Fig. S2 in the supplemental material.

respectively, which could be used for diffraction angle calibration. The blue dashed lines show positions of diffraction peaks along the 2θ direction from the shock-compressed Ta. Three diffraction lines of shock-compressed Ta, i.e., Ta(110), Ta(200), and Ta(211), have been observed in this image. Blue arrows marked the positions of dynamic Ta(200) signals.

temperature, our dynamic compression results extend this conclusion to 318 GPa. Crucially, even without structural refinement, the detection of multiple diffraction peaks—Ta(110), Ta(200), and Ta(211)—at 131 GPa directly confirms the BCC symmetry, as shown in Fig. 4. This multi-peak evidence strengthens the structural assignment compared to the result of Kraus et al.[8]. The absence of orthorhombic phase signatures, combined with Hugoniot-constrained structural modeling, conclusively demonstrates that tantalum retains its BCC lattice until shock melting occurs. These

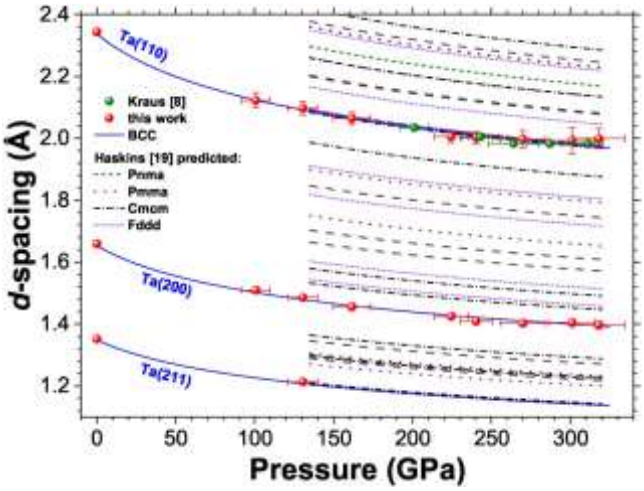

FIG. 6. The relationship between d-spacing and pressure for shock-compressed tantalum. The vertical axis covered the 2θ range of DXRD. Experimental data were represented by red (this work) and green (Ref. 8) solid circles. The blue solid line corresponded to the BCC structure. The reference orthorhombic structures came from Ref. 19. Green dashed lines represented the Pnma structure, while purple short dashed lines represented the Pmma structure. The black dashed dotted lines represented the Cmcm structure, and the violet dotted lines represented the Fddd structure.

findings resolve uncertainties arising from theoretical predictions of high-pressure polymorphism[19,29,31] and establish a robust experimental basis for interpreting tantalum's melting curve.

Vol. 13 No. 2 | Imp. Factor: 8.13
DOI: https://doi.org/10.5281/zenodo.15845923

Our experiments successfully detected at least two dynamic diffraction peaks. The 10 kJ-class laser facility generated a lower background environment, enhancing detection sensitivity for weak diffraction signals. This advantage allowed us to balance signal intensity and resolution without compromising data reliability. A reduced sample-to-detector distance in the DXRD improved the detection limit, albeit at the cost of angular resolution. We prioritized multi-peak detection over resolution, as resolving multiple reflections provides direct structural evidence even with moderate resolution. Thin foils were prone to strong texture due to grain orientation alignment during fabrication. To minimize this, we employed optimized target fabrication protocols, including controlled rolling and annealing, to reduce preferred crstallographic orientations. This enabled the detection of higher-order peaks despite residual texture. Our pulsed x-ray source, with lower intensity compared to OMEGA laser experiments,[72] generated weaker plasma heating in the sample. This likely suppressed the DW effect, as indicated by the retained sharpness of diffraction peaks even at 318 GPa. These design choices provide a technical framework for detecting weak diffraction signals under high-temperature and high-pressure conditions, particularly in systems where texture and thermal effects dominate.

Table I summarized the experimental data from this study. In the shock pressure range of 101–240 GPa, we consistently observed at least two high-pressure diffraction peaks in shocked tantalum. Notably, at 131 GPa (Fig. 4), three diffraction peaks were detected. Partial melting was first observed at 270 GPa, indicated by a diffuse scattering feature at the Ta(110) scattering angle. The full width at half maximum (FWHM) of this feature increased from 2 to 3.5, while the solid peak intensity decreased, signaling the onset of melting along the principal Hugoniot. Similar mixed-phase diffraction signatures appeared at 301 and 318 GPa. Above 318 GPa, solid diffraction peaks disappeared entirely, leaving only a broad diffuse scattering feature. At these higher pressures, the FWHM increased significantly (5:5) compared to lower pressures (2). Regrouped diffraction images at 101, 162, 240, 270, 318, and 356 GPa were provided in Sec. S3 of the supplementary material.

B. Melting curve of BCC tantalum from abinitio molecular dynamics

We determined the melting temperature at four pressures, corresponding to atomic volumes of 15.332, 12.771, 10.906, and 9.995 Å^3. Table II summarized the simulated melting points, including temperature, pressure, energy, lattice constant, and mass density for

TABLE II. AIMD simulation results of BCC tantalum under various volumes. T_m and P were the melting temperature and pressure of the system at volume V_0, respectively. E was the unit atomic energy of the system in the equilibrium state. a_0 and ρ were the lattice constant and mass density of tantalum, respectively. Statistical deviations of the calculated P, T_m, and E were presented.

a_0 (Å)	V_0 (Å^3)	ρ (g/cm^3)	P (GPa)	T_m (K)	E/atom (eV)
			73 ± 0.5	5206 ± 120	−10.39 ± 0.04
3.130	15.332	19.603			
2.945	12.771	23.534	179 ± 0.6	7650 ± 198	−8.50 ± 0.03
2.794	10.906	27.560	329 ± 1	9905 ± 256	−5.77 ± 0.05
2.714	9.995	30.069	449 ± 284	11436 ±	−3.68 ± 0.05

Vol. 13 No. 2 | Imp. Factor: 8.13
DOI: https://doi.org/10.5281/zenodo.15845923
BCC tantalum at each volume. To model the high-pressure melting curve, we used the Simon–Glatzel equation T ¼ T_{mo}(P=a+1)^{b} with parameters a ¼ 49, b ¼ 0:54, and T_{mo} ¼ 3268:8 K. The predicted ambient melting temperature closely matches experimental values of 3268– 3280 K.[12–14] Further simulation details were provided in Sec. S4 of the supplemental material.

Figure 1 compared our melting curve with experimental data[8–16] and previous theoretical results.[19–23] First, a clear discrepancy exists between dynamic and static experiments. Melting curves extrapolated from recent static experiments[14,16] were lower than those obtained from shock compression experiments.[8–11] Second, DFT-based predictions (this work and Refs. 20 and 19) show significantly less dispersion under high pressure than those derived from the extended Finnis–Sinclair (EFS) and embedded atom method (EAM) Ta2 potentials,[21,22] as well as other approaches.[8,23] Third, theoretical results,[19,20] including our study, align more closely with dynamic experiments. Given the experimental uncertainties, the broad spread of melting curves highlights the challenge of constructing an accurate multi-phase equation-of-state.

The characteristics of the melting data in Fig. 1 can be understood from two perspectives. First, the discrepancies between dynamic and static experiments primarily stem from the complexity of experimental methods. Second, the dispersion in theoretical results depends largely on the reliability of high-pressure melting simulations and the choices of interaction potentials.

Our study presents the first melting curve of tantalum obtained entirely through AIMD, without relying on auxiliary reference or optimized potentials. As shown in Fig. 1, our results align well with the theoretical calculations of Taioli et al.[20] and Haskins and Moriarty.[19] Taioli et al.[20] used DFT-based thermodynamic perturbation theory to calculate the melting curve of tantalum. Haskins et al.[18,19] extensively investigated tantalum's polymorphism and melting under high pressure using the two-phase and Z-method, employing MGPT (version Ta6.8x) molecular dynamics with cell sizes of approximately 80 000 atoms to account for size effects. These studies represent two of the most reliable firstprinciples theoretical results available.

In contrast, Ravelo et al.[21] developed two EAM potentials (Ta1,Ta2) for tantalum, fitted to experimental and DFT data, and simulated melting curves in a nonequilibrium regime using the EAM Ta2 potential with 16 000 atoms. While their results agree with high-melting static experiments,[16] they deviate from DFT-based equilibrium simulations under high pressure (this work and Refs. 20 and 19). Wang et al.[22] and Liu et al.[28] employed EFS potential[73] with the modified-Z and two-phase methods, respectively, using supercells of 960 and 1792 atoms. Although their melting curves show similar accuracy, EAM Ta2 and EFS potentials were considered unreliable for a broad range of pressures and temperatures, as they were fitted based on limitted parameters.

The melting curves reported by Kraus et al.[8] and Gorman et al.[23] shown significant discrepancies. The melting curve of Kraus et al.[8] deviates notably in slope from the theoretical results of Taioli et al.,[20] Haskins and Mortiarty,[19] and this work, as well as from melting temperatures measured in both dynamic and static compression experiments,[10,11,13–15] as shown in Fig. 1. The inferred shock melting temperature could not fully reconcile the differences between static and dynamic high-pressure data. Gorman et al.[23] reported a lower melting curve than those previously mentioned. This discrepancy arises from the limitations of using cold or isentropic curves, which were less effective in constraining the hightemperature physical properties of tantalum.

C. Shock melting of tantalum from experiment and theory

The shock melting pressure range was determined by the intersection of the Hugoniot and the melting curve. In dynamic experiments, this range can be identified by observing changes in sound velocity or the crystal structure.

Vol. 13 No. 2 | Imp. Factor: 8.13
DOI: https://doi.org/10.5281/zenodo.15845923

dynamic experiments.[7,9] The blue, magenta, and wine dashed lines

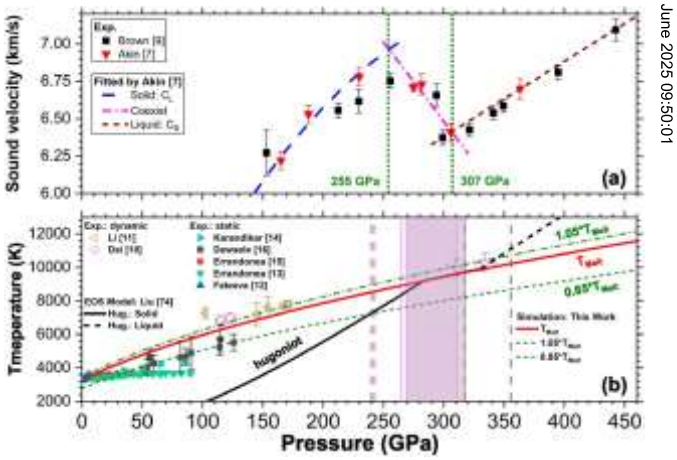

Figure 7(a) presented high-pressure sound velocity data from

FIG. 7. (a) Sound velocity measured by Akin et al.[7] and Brown and Shaner.[9] Blue, magenta, and wine dashed lines were the fitting of data of Akin et al.. Green short dashed lines marked the intersection of fitted lines, which represented the shock melting pressures from light gas gun experiment. (b) The proposed melting curve of this work. The solid red line represented the tantalum melting curve fitted by the simulation results in this work, while the green dotted dashed and dashed lines above and below the melting curve correspond to deviation boundary of the melting curve, upward by 5% and downward by 15%, respectively. Gray dashed lines and magenta dashed lines marked the pressures for the highest solid phase and the lowest liquid phase measured in this work and by Kraus et al.,[8] respectively. Light gray and magenta shading marked the pressure range of the solid –liquid mixture phase measured by this work and Kraus et al.[8]

represent fitted trends based on Akin et al.[7] The melting transition pressure in the shock melting regime was identified at the intersections of these lines, defining a transition range between 255 and 307 GPa. This result aligned with Akin et al.,[7] where shear modulus softening was observed at 250 GPa, and melting occurred at 300 GPa.

Figure 7(b) compared our melting curve with representative dynamic[10,11] and static[12–16] melting temperature measurements. To analyze the shock melting pressure range from in situ x-ray diffraction data, we have marked key pressure ranges in Fig. 7(b) based on experimental results. The magenta and gray dashed vertical lines indicate the highest pressure for the solid phase and the lowest pressure for the liquid phase, as determined by Kraus et al.[8] and this work, respectively. The shaded magenta and gray regions represent the solid–liquid coexistence. As shown in Fig. 7(b), a discrepancy persist between static and dynamic experiments. Our theoretical melting curve algins more closely with dynamic experiments than with static ones, with deviations of approximately 5% (green dotted dashed line) and 15% (green dashed line), respectively. Given experimental uncertainties, most dynamic[10,11] and static[12,16] data support our findings. This suggests that the tantalum melting curve has a steeper pressure-dependent slope rather than the flatter trend reported in previous studies.[13,15,17]

The shock melting pressure range of tantalum can be inferred from experimental data. Our results indicate that shock melting occurred between 270 and 318 GPa, as detailed in Sec. S3 of the supplemental material. At 318 GPa, in situ x-ray diffraction revealed a distinct solid–liquid coexistence signature, establishing the upper boundary of the shock melting transition at or above this pressure. By analyzing the pressure range derived from sound velocity data in Fig. 7(a), we conclude that shock

Vol. 13 No. 2 | Imp. Factor: 8.13
DOI: https://doi.org/10.5281/zenodo.15845923
melting occurs between 255 and 318 GPa, corresponding to melting temperatures of 8754 + 226 and 9698 + 251 K, respectively. Our conclusions regarding the shock melting pressure range was in agreement with the results of Kraus et al.[8]

As a reference, we used the wide regime equation of state (WEOS) model[74] to calculate the Hugoniot of tantalum at the pressure–temperature plane. The liquid phase Hugoniot was estimated by adjusting the solid Hugoniot with melting entropy. Melting entropy was determined using two methods. The first method employed a semi-analytical approximation,[75] defining melting entropy as the entropy difference between 255 and 318 GPa: $\Delta S \approx 2C_V \ln(U_{p2}/U_{p1}) - 0.9R$, where U_{p1} and U_{p2} were particle velocities at 255 and 318 GPa, respectively, with $C_V \approx 3R$ at Dulong– Petite limit and R as the gas constant. The second method estimated melting entropy using the energy change along an isochore: $E_M \approx T_M \Delta S$, based on AIMD simulations. Both methods yielded consistent results, confirming $\Delta S \approx 0.9R$, which was then applied as a melting entropy correction in WEOS-based shock melting calculations. We evaluated the impact of ΔS on melting temperature and pressure, finding that for every 0:1R change in entropy, pressure varied by 5 GPa and temperature by 60 K. According to the WEOS model, the predicted shock melting pressure range was 48 GPa (282–330 GPa), compared to the experimentally deduced 63 GPa (255–318 GPa). These values were nearly equal within the experimental error. However, the WEOS model tends to overestimate shock melting pressure, suggesting a higher melting temperature.

Section S5 of the supplemental material presented a comparison between the WEOS model and experimental pressure–density data, showing good agreement. For more accurate Hugoniot and melting temperature predictions, thermal contributions from ions and electrons, as well as the solid–liquid phase transition, should be incorporated into the WEOS model.

The melting transition range derived from two independent laser-driven experiments—this work and Kraus et al.[8] show agreement with microsecond—timescale sound velocity measurements conducted using gas gun[7] and chemical explosive platforms.[9] Additionally, the solid–liquid coexistence intervals obtained from these experiments across different time scales algin well with those inferred from equilibrium AIMD simulation combined with the WEOS model. This consistency suggested that nonequilibrium effects have a limited impact on the melting process.

IV. CONCLUSION

In conclusion, this study provides a detailed characterization of the high-pressure melting behavior of tantalum through a combined experimental and theoretical approach. In situ x-ray diffraction experiments under shock compression up to 318 GPa confirmed the persistence of the BCC structure, with unambiguous detection of higher-order reflections, including Ta(200) and Ta (211), beyond the previously reported Ta(110). Pressure-dependent d-spacing analysis conclusively ruled out previously proposed orthorhombic phases (Pnma, Pmma, Cmcm, and Fddd). To determine the melting curve, a first-principles molecular dynamics framework was developed without reliance on empirical potentials. The resulting Simon–Glatzel equation parameters ($a \approx 49$, $b \approx 0.54$, and $T_{mo} \approx 3268.8$ K) yield an ambient pressure melting temperature consistent with established experimental measurements. The shock melting pressure range (255–318 GPa) was further validated through both x-ray diffraction and sound velocity data, demonstrating agreement with prior work by Kraus et al. [8] Analysis based on a WEOS model highlighted the significant contribution of melting entropy (ΔS 0:9R) to reconciling theoretical predictions and experimental results. The integration of in situ x-ray diffraction and AIMD simulations establishes a reliable framework for high-pressure melting phenomena. This methodology reduces dependence on empirical assumptions and is transferable to

Vol. 13 No. 2 | Imp. Factor: 8.13
DOI: https://doi.org/10.5281/zenodo.15845923
other metallic materials, offering a pathway to address persistent discrepancies between dynamic and static compression experiments.

SUPPLEMENTARY MATERIAL

See the supplementary material for additional information on the experimental setup, data analysis, and results.

ACKNOWLEDGMENTS

We express our sincere gratitude to Qili Zhang, Bo Sun, Mingfeng Tian, Qing Ye, Chen Zhang, Chaoyang Li, and Yang Cai for their valuable comments and suggestions. We would also like to acknowledge and thank the operation team of the 10 kJ-class Laser Facility at LFRC for their invaluable support in laser operation and technical assistance throughout the laser experiments. Additionally, we extend our appreciation to the target fabrication department at LFRC for their expert assistance. This work was carried out with the support of the National Natural Science Foundation of China (NSFC) (Grant Nos. 12074351, U2230401, 12205276, 12174354, and 12135019), the Applied Fundamental Research in Sichuan Province (Grant No. 2021YJ0527), and the foundation of Laboratory of Computational Physics. We would like to express our gratitude for the generous funding provided by these grants, which has enabled us to conduct this research and improven our understanding of the melting behavior of tantalum under high pressure. Furthermore, we would like to thank the Tianhe platforms at the National Supercomputer Center in Tianjin for their support. Their computational resources have been instrumental in our research endeavors.

AUTHOR DECLARATIONS

Conflict of Interest

The authors have no conflicts to disclose.

Author Contributions

Hao Liu and Hongzhou Song contributed equally to this work.

Hao Liu: Conceptualization (equal); Formal analysis (equal);
Investigation (equal); Methodology (equal); Visualization (equal); Writing – original draft (equal); Writing – review & editing (equal). Hongzhou Song: Writing – original draft (equal). Huan Zhang: Writing – review & editing (supporting). Xiaoxi Duan: Writing – review & editing (supporting). Tingting Zhang: Investigation (equal); Writing – review & editing (supporting). Haifeng Liu: Conceptualization (equal); Supervision (lead); Writing – original draft (equal). Zhebin Wang:
Conceptualization (equal); Investigation (equal); Project administration (equal); Supervision (equal). Yu Liu: Writing – review & editing (equal). Shuaichuang Wang: Methodology (equal). Yulong Li: Writing – review & editing (supporting). Liang Sun: Writing – review & editing (supporting). Weiming Yang: Writing – review & editing (supporting). Zanyang Guan: Data curation (supporting); Investigation (supporting). Gongmu Zhang: Conceptualization (supporting); Project administration (supporting). Dong Yang: Writing – review & editing (supporting). Jiamin Yang: Writing – review & editing (supporting). Zongqing
Zhao: Project administration (supporting); Writing – review & editing (supporting). Haifeng Song: Methodology (supporting); Writing – review & editing (supporting). Yongkun Ding: Supervision (equal); Writing – review & editing (supporting).

DATA AVAILABILITY

The data that support the findings of this study are available from the corresponding authors upon reasonable request.

REFERENCES

Vol. 13 No. 2 | Imp. Factor: 8.13
DOI: https://doi.org/10.5281/zenodo.15845923

Albertazzi, B., Ozaki, N., Zhakhovsky, V., Faenov, A., Habara, H., Harmand, M., Hartley, N., Ilnitsky, D., Inogamov, N., Inubushi, Y., Ishikawa, T., Katayama, T., Koyama, T., Koenig, M., Krygier, A., Matsuoka, T., Matsuyama, S., McBride, E., Migdal, K. P., … Kodama, R. (2017). Dynamic X-ray diffraction measurement of shocked iron up to 170 GPa. Science Advances, 3(7), e1602705. https://doi.org/10.1126/sciadv.1602705

Wehrenberg, C. E., McGonegle, D., Bolme, C. A., Higginbotham, A., Lazicki, A., Lee, H. J., Nagler, B., Park, H.-S., Remington, B. A., Rudd, R. E., Sliwa, M., Suggit, M. S., Swift, D. C., Tavella, F., Zepeda-Ruiz, L., & Wark, J. S. (2017). Crystal growth in shock-compressed SiO_2. Nature, 550(7677), 496–499. https://doi.org/10.1038/nature24052

Zhang, Y., Yang, C., Alatas, A., Said, A. H., Salke, N. P., Hong, J., & Lin, J.-F. (2019). Phonon density of states of iron under high pressure. Physical Review B, 100(7), 075145. https://doi.org/10.1103/PhysRevB.100.075145

Katagiri, K., Ozaki, N., Ohmura, S., Albertazzi, B., Hironaka, Y., Inubushi, Y., Ishida, K., Koenig, M., Miyanishi, K., Nakamura, H., Nishikino, M., Okuchi, T., Sato, T., Seto, Y., Shigemori, K., Sueda, K., Tange, Y., Togashi, T., Umeda, Y., … Kodama, R. (2021). Shock compression of Fe–Ni–Si alloy and its implications for planetary cores. Physical Review Letters, 126(17), 175503. https://doi.org/10.1103/PhysRevLett.126.175503

Akin, M. C., Nguyen, J. H., Beckwith, M. A., Chau, R., Ambrose, W. P., Fat'yanov, O. V., Asimow, P. D., & Holmes, N. C. (2019). Equation of state of iron from shock compression and release. Journal of Applied Physics, 125(14), 145903. https://doi.org/10.1063/1.5091790

Kraus, R. G., Coppari, F., Fratanduono, D. E., Smith, R. F., Lazicki, A., Wehrenberg, C., Eggert, J. H., Rygg, J. R., & Collins, G. W. (2021). Shock vaporization of iron and implications for planetary cores. Physical Review Letters, 126(25), 255701. https://doi.org/10.1103/PhysRevLett.126.255701

Brown, J., & Shaner, J. (1984). Dynamic compression of solids. In Shock Waves in Condensed Matter 1983 (pp. 91–94). Elsevier.

Dai, C., Hu, J., & Tan, H. (2009). The effects of temperature on the resistance of metallic nanowires. Journal of Applied Physics, 106(4), 043519. https://doi.org/10.1063/1.3204494

Li, J., Zhou, X., Li, J., Wu, Q., Cai, L., & Dai, C. (2012). A laser-driven flyer plate impact system for shock compression experiments. Review of Scientific Instruments, 83(5), 053902. https://doi.org/10.1063/1.4711126

Fateeva, N. S., & Vereshchagin, L. F. (1971). Compressibility of metals at high pressures. Soviet Physics Doklady, 16, 322–323.

Errandonea, D., Schwager, B., Ditz, R., Gessmann, C., Boehler, R., & Ross, M. (2001). Systematics of transition metal melting. Physical Review B, 63(13), 132104. https://doi.org/10.1103/PhysRevB.63.132104

Vol. 13 No. 2 | Imp. Factor: 8.13
DOI: https://doi.org/10.5281/zenodo.15845923

Karandikar, A., & Boehler, R. (2016). A new approach to calibrate and check high-pressure devices. Physical Review B, 93(5), 054107. https://doi.org/10.1103/PhysRevB.93.054107

Errandonea, D., Somayazulu, M., Häusermann, D., & Mao, H. K. (2003). Melting of metals at high pressures. Journal of Physics: Condensed Matter, 15(45), 7635–7649. https://doi.org/10.1088/0953-8984/15/45/012

Dewaele, A., Mezouar, M., Guignot, N., & Loubeyre, P. (2010). High-pressure-high-temperature equation of state of periclase from synchrotron X-ray diffraction measurements. Physical Review Letters, 104(25), 255701. https://doi.org/10.1103/PhysRevLett.104.255701

Ruiz-Fuertes, J., Karandikar, A., Boehler, R., & Errandonea, D. (2010). High-pressure melting curve of Ge. Physics of the Earth and Planetary Interiors, 181(1–2), 69–72. https://doi.org/10.1016/j.pepi.2010.05.005

Haskins, J. B., Moriarty, J. A., & Hood, R. Q. (2012). First-principles equation of state and shock compression predictions for aluminum. Physical Review B, 86(22), 224104. https://doi.org/10.1103/PhysRevB.86.224104

Haskins, J. B., & Moriarty, J. A. (2018). Ab initio equations of state and shock Hugoniot predictions for Fe, Ni, and Fe–Ni alloys. Physical Review B, 98(14), 144107. https://doi.org/10.1103/PhysRevB.98.144107

Taioli, S., Cazorla, C., Gillan, M. J., & Alfè, D. (2007). Melting curve of bcc iron from first principles simulations. Physical Review B, 75(21), 214103. https://doi.org/10.1103/PhysRevB.75.214103

Ravelo, R., Germann, T. C., Guerrero, O., An, Q., & Holian, B. L. (2013). Shock-induced plasticity in tantalum single crystals: Atomistic simulations. Physical Review B, 88(13), 134101. https://doi.org/10.1103/PhysRevB.88.134101

Wang, S., Liu, H., Zhang, G., & Song, H. (2013). A study of equation of state of aluminum by ab initio calculations. Journal of Applied Physics, 114(16), 163514. https://doi.org/10.1063/1.4826443